Research on Chemical Intermediates (2023) 49:589–601
https://doi.org/10.1007/s11164-022-04883-7

Facilely preparing lignin-derived graphene-ferroferric oxide nanocomposites by flash Joule heating method

Yun Chen[1] · Zilin He[1] · Shuquan Ding[1] · Meng Wang[2] · Huilong Liu[1] · Maoxiang Hou[1] · Xin Chen[1] · Jian Gao[1] · Lixi Wang[2] · Ching-Ping Wong[3]

Received: 21 July 2022 / Accepted: 14 November 2022 / Published online: 24 November 2022

Abstract

Lignin is the most abundant renewable aromatic polymer in nature; however, its full potential for conversion to high-value materials for practical applications is yet to be explored. Herein, a flash Joule heating process that enables the efficient conversion of lignin into a graphene-based nanocomposite is demonstrated. This method leverages the mixing of lignin with a ferric trichloride ($FeCl_3$) solution to allow the insulated lignin to be conductive, thus producing an instantaneous high-temperature and high-pressure environment through electrical flash Joule heating. This efficiently converts the cheap carbon source into graphene and in situ loads ferroferric oxide (Fe_3O_4) nanoparticles onto the graphene flakes. Importantly, the prepared graphene/Fe_3O_4 nanocomposites were naturally endowed with electromagnetic wave absorption properties. The developed method eliminates the need for multistep processes and expensive equipment and shows broad prospects for facile processing of functional materials from low-value carbon sources.

Keywords Graphene/Fe_3O_4 nanocomposites · Flash Joule heating · Electromagnetic wave absorption · Lignin-derived graphene

✉ Yun Chen
chenyun@gdut.edu.cn

✉ Lixi Wang
wanglixi@njtech.edu.cn

[1] State Key Laboratory of Precision Electronic Manufacturing Technology and Equipment, Guangdong University of Technology, Guangzhou 510006, China

[2] College of Materials Science and Engineering, Nanjing Tech University, Nanjing 210009, China

[3] School of Materials Science and Engineering, Georgia Institute of Technology, Atlanta, GA 30332, USA

Introduction

Lignin is the most abundant renewable natural aromatic polymer in the world [1, 2]. The dry weight of lignin found in most terrestrial plants is approximately 15–40%, which is regarded as an ideal precursor of carbon materials [3, 4]. Moreover, lignin is the main component of black liquor in papermaking chemical waste. It is estimated that only 2% of the 50 million tons of lignin isolated from the process of pulping was used for personalized utilization [5, 6]. Therefore, developing a new route to promote the conversion of lignin into high-value materials is of great significance.

Theoretically, lignin can be used as a raw material for the preparation of graphene. Among the preparation methods of graphene, the more mature ones are mechanical stripping [7, 8], redox method [9–11], and chemical vapor deposition (CVD) [12, 13]. However, only a few studies have successfully converted lignin into graphene, these include hydrothermal reforming method with long time (more than 12 h) and low efficiency [14, 15], CVD methods with expensive equipment [16], and carbonization methods with low efficiency [17]. In addition, these methods require cumbersome process, lengthy processing time, expensive equipment, and strong oxidants that are harmful to the environment. Although the laser irradiation method for thin-film manufacturing has been developed in recent years [18–23], it is still unable to efficiently prepare graphene on a large scale.

Recently, a novel processing method called flash Joule heating (FJH) has been reported, which can utilize a variety of raw materials to prepare graphene [24, 25]. During the flash Joule heating processing, by using the transient discharge of a capacitor bank, the environment in which the material is processed will instantly rise to extremely high temperatures and pressures due to the Joule heating effect, resulting in processing products that are unmatched by conventional processing methods [26]. For example, holey and wrinkled flash graphene (HWFG) was processed from waste plastics using the FJH method, and HWFG was capable to be a stable catalyst in the metal-free hydrogen evolution reaction [27]; similarly, turbostratic flash graphene (tFG) was processed from waste rubber and was added into cement to improve the compressive strength [28]. However, this FJH method's premise in successfully preparing high-quality graphene is that the carbon source to be processed needs to have good conductivity. Therefore, when dealing with carbon sources that typically have poor conductivity, highly conductive and expensive additives must be added, such as carbon black [24, 25].

Consequently, when processing lignin by FJH method, it needs to find an additive that is inexpensive and helps to improve the value of lignin. Adding iron solution to lignin is a good choice. Because the iron solution is facile to obtain and has good electrical conductivity, moreover, the presence of iron in the flash-induced graphene has the advantage of high saturation magnetization and high permeability, which can attenuate electromagnetic waves by magnetic loss and has good wave absorption properties [29–31], thereby, significantly improving the utilization value of the product.

In this study, through mixing of lignin with a ferric chloride solution to allow the insulated lignin to be conductive, an instantaneous high-temperature and

high-pressure environment wad produced through electrical flash Joule heating under which high-quality graphene can be obtained, which is called lignin-derived graphene (L-FG). In addition, taking advantage of reducing the ferric ions (Fe^{3+}) in the salt solution during the flash Joule heating process, Fe_3O_4 nanoparticles were uniformly loaded in situ in the porous L-FG, which is naturally suitable for electromagnetic wave absorption. Compared with the previously reported flash Joule heating method, the developed method can convert poor conductivity raw materials into high-quality graphene-based materials, showing potential application prospects in material processing.

Experimental section

Materials

The sodium lignosulfonate used in this study was purchased from Fuyang Manlin Biotechnology Co., Ltd; to simulate the $FeCl_3$ in seawater, solute $FeCl_3{\cdot}6H_2O$ purchased from Alfa aesar company was used. During the experiments, $FeCl_3{\cdot}6H_2O$ and deionized water were mixed to form a uniform activation solution with a specific concentration. Then, a certain amount of sodium lignosulfonate and $FeCl_3$ solution were taken to stir in a mortar to form a paste, which was used as the carbon source.

Methods

A piece of self-developed discharge equipment was used in this study, mainly including a high-voltage power supply, an electrical cabinet, a vacuum chamber, and a vacuum pump. First, the mixture of lignin and $FeCl_3$ solution (25wt%) was prepared and placed in a quartz tube that was installed in the vacuum chamber. The outer and inner diameter of the quartz glass tube is 20 mm and 10.2 mm, respectively. Subsequently, two copper electrodes with a diameter of 10 mm were assembled at both ends of the quartz tube. The other ends of these two copper electrodes were connected to the two poles of the capacitor bank in the electrical cabinet, respectively. The capacitor bank consists of 12 mF and 36 mF sub-capacitors for a total of 240 mF. After charging the capacitor bank with the high-voltage power supply with a maximum voltage of 1000 V, the charging circuit was switched off, and the discharge circuit was switched on sequentially. In this way, a large number of the charge stored in the capacitor bank quickly flowed through the lignin/$FeCl_3$ mixture, and discharged to produce an extreme high-temperature and high-pressure environment, resulting in the desired products.

Characterization

A scanning electron microscope (SEM, SU8220, Hitachi, Japan) was used to study the morphology of F-LG/Fe_3O_4. Raman spectroscopy was performed by a Raman microscope (Raman, LabRAM HORIBA France) excited with a 532 nm laser at

room temperature. Powder products were dispersed by ultrasonic and transferred to the microgrid carbon film, and the micromorphology of F-LG/Fe_3O_4 was examined by TEM (FEI Tecnai G2 F20). X-ray energy dispersive spectroscopy (EDS) was used to analyze the elemental composition and distribution. X-ray photoelectron spectrometer (XPS, Thermo Fisher Scientific K-Alpha) was used to characterize the elemental composition and content of L-FG/Fe3O4; during the analysis, the vacuum degree in the analysis chamber was better than 2×10^{-9} mBar, x-ray source (the beam spot of the Al target was 400 μm, the voltage and current were 15 kV and 10 mA, respectively, and the covalent C1s peak (284.8 eV) was used as the reference to correct the spectral data. X-ray diffraction (XRD) spectrometry was recorded on a Bruker D8 Advance x-ray diffractometer equipped with a diffracted-beam monochromator set for Cu Ka radiation ($\lambda = 1.5418$ Å) to analyze the chemical composition of the elements contained. Atomic force microscopy (AFM, Bruker Dimension FastScan) was performed to measure the thickness of graphene.

The EM parameters were measured by using a vector network analyzer (E5071C, Agilent, USA) from 2 to 18 GHz. The as-prepared samples and paraffin wax were homogeneously mixed in a mass ratio of 7: 3, and then pressed into toroidal rings ($\phi_{out} = 7.00$ mm, $\phi_{in} = 3.04$ mm).

Results and discussion

Preparation and characterizations of F-LG/Fe_3O_4

Figure 1A shows a schematic illustration of the preparation of F-LG/Fe_3O_4. Raw lignin is not conducive to processing by flash Joule heating due to the poor conductivity, however, iron has been reported to induce graphitization in solid carbon materials in situ during pyrolysis and increase the capacitance of graphite by two orders of magnitude [21], through mixing of lignin with a ferric chloride solution to allow the insulated lignin to be conductive, it is possible to obtain high-quality graphene under an instantaneous high-temperature and high-pressure environment created by the electrical flash Joule heating method. Therefore, it is proposed that mixing lignin with $FeCl_3$ solution and followed by electrical-flashed in the confined space, because of the existence of an external electric field, the ions in the mixture can move directionally in the wet mixture (Fig. 1b), herein, a conductive path through ion transport is believed to be formed, producing a large amount of joule heat in lignin. Thus, an extremely high-temperature and high-pressure environment is created, under which Fe^+ and Cl^- are inserted between the carbide layers, resulting in the rapid conversion of lignin into high-quality graphene (Fig. 1c).

To prove the hypothesis, fabricating F-LG was proceeded on the self-developed discharge equipment (Fig. 1d). After 350 mg of lignin was mixed with 150 μL $FeCl_3$ solution, the mixture was placed into the discharge equipment which was switched on subsequently, therefore, a large amount of the charge quickly flowed through the lignin/$FeCl_3$ mixture, discharged to produce an extreme high-temperature and high-pressure environment due to the Joule heating effect (Fig. 1e). Because of the high temperature produced by discharge, $FeCl_3$ first reacted with water in the raw

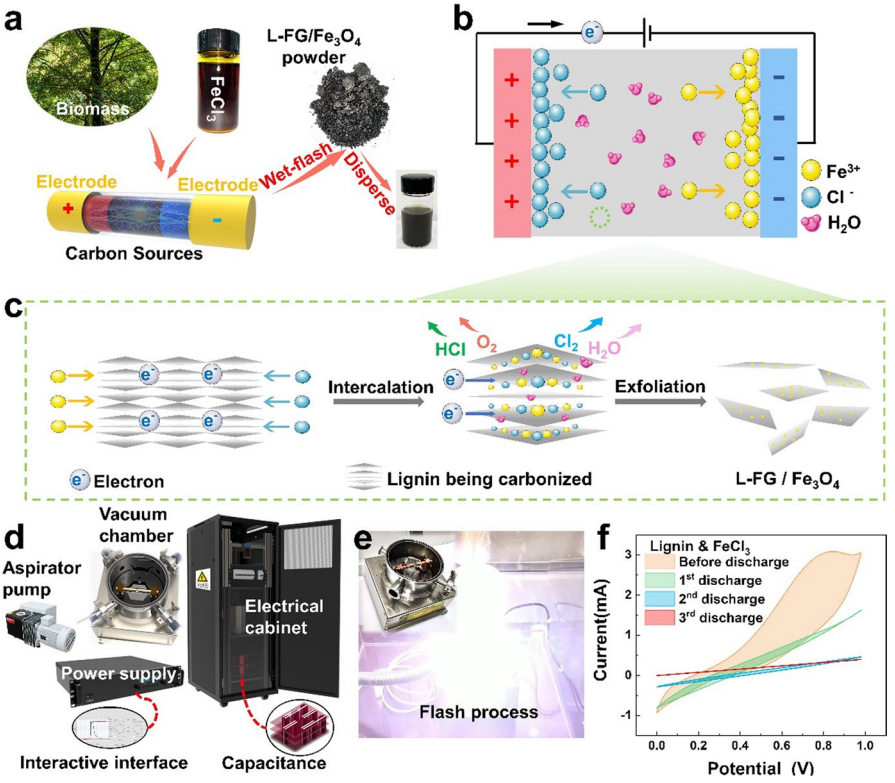

Fig. 1 Process and setup of flash Joule heating. **a** concept of preparing graphene Fe_3O_4 nanocomposites through flash Joule heating; **b** The cations and anions move directionally during the flash Joule heating process; **c** Electron and ion transport co-existed during the flash Joule heating process; **d** Self-developed electrical flash Joule heating equipment; **e** The flash at the discharge moment created a high-temperature and high-pressure environment in the quartz tube; **f** Capacitance in a quartz tube changes with discharge cycles

material to produce ferric hydroxide ($Fe(OH)_3$) and irritating colorless gas hydrogen chloride (HCl), as shown in Eq. 1:

$$FeCl_3 + 3H_2O \xrightarrow{>1800K} Fe(OH)_3 + 3HCl \uparrow \quad (1)$$

Simultaneously, the produced HCl gas was pumped out of the quartz tube using a vacuum pump. As the carbonization process proceeded, the carbides gradually increased, resulting in a gradual decrease in resistance; thus, the electrons freely moved along the paths formed by the carbides (electron transport path). Therefore, the carbides were gradually peeled off to produce L-FG. It was observed that before the final discharge-induced flash, after the first three pure discharges, the capacitance of the activated mixture of ferric chloride and lignin decreased successively, and after the first and second discharge cycles, the current–voltage (CV) curves still maintained a pseudo rectangle (Fig. 1f), indicating a typical double-layer capacitance behavior and ion transport path in the wet-flash processing. It should be

mentioned that the capacitance approached zero at the third discharge (Fig. 1f), as all the water in the mixture was evaporated by the high temperature, causing the discharge, only dry carbides were left. It was found that when the capacitance of the raw material was 0, the discharge produced dazzling white light, which means that the local temperature in the quartz tube reached at least 3000 K. As the temperature was higher than 1800 K, the produced $Fe(OH)_3$ was unstable and decomposed into ferric oxide (Fe_2O_3) and vapor, as shown in Eq. 2:

$$Fe(OH)_3 \xrightarrow{\Delta} Fe_2O_3 + 3H_2O \uparrow \quad (2)$$

The produced Fe_2O_3 continued to decompose into oxygen and Fe_3O_4, which is the stable form of iron oxide at high temperatures, as shown in Eq. 3:

$$6Fe_2O_3 \xrightarrow{\Delta} 4Fe_3O_4 + O_2 \uparrow \quad (3)$$

Therefore, the total equation for this process can be rewritten as Eq. 4:

$$12FeCl_3 + 18H_2O \xrightarrow{>1800K} 4Fe_3O_4 + 36HCl \uparrow + O_2 \uparrow \quad (4)$$

Previous reports on solvent-free flash processing called this carbonization process before stripping as a simple preheating treatment [32], which is a single-electron transport mechanism. However, during the processing reported in this study, the ion transport path was introduced, thus accelerating the carbonization process.

To verify that graphene was formed after flash Joule heating processing, Raman characterizations were performed. Raman spectra (Fig. 2a) showed that there were three main peaks in the spectra of L-FG, the *D* peak at 1336 cm^{-1}, the *G* peak at 1578 cm^{-1}, and the 2*D* peak at 2680 cm^{-1} [33]. In Raman spectroscopy, the ratio of *D*-peak to *G*-peak of graphene is related to the surface defects, and the lower the ratio, the fewer the defects of graphene; the shape of the 2*D* peak is related to the number of layers of graphene, and the higher the intensity and narrower the half-peak width, the fewer the corresponding layers of graphene. For the produced L-FG, the ratio of the *D* peak intensity to the *G* peak intensity (I_D: I_G) was 0.56, and the ratio of the 2*D* peak intensity to the *G* peak intensity (I_{2D}: I_G) was as high as 1.5. By matching the shape of the 2*D* peak and referring to the ratio of the 2*D* peak to the *G* peak, it can be inferred that the L-FG with the least layers corresponds to single-layer graphene [33–35]. After spectral fitting and systematic analysis, it was noted that there was a peak at 1778 cm^{-1} in the 1650–1800 cm^{-1} band, which is called the M band caused by an intra-valley double resonance scattering process (Fig. 2b), indicating that Bernal (AB type) stacking exists in the L-FG [36, 37]; peaks were observed at 1897 cm^{-1} and 2040 cm^{-1}, which indicated that there was a turbine-like stacking in the L-FG [36, 38], which is consistent with a previous report [39]. In terms of studying the effects of charging voltage on the processed products, it was found that when the voltage was 160 V, the I_D/I_G reached a minimum value (Fig. 2c, d), which indicated that the product was a type of three-dimensional graphene with the fewest defect. Meanwhile, when the voltage was increased from 120 to 180 V, I_{2D}/I_G increased, indicating a higher quality graphite structure was formed; when

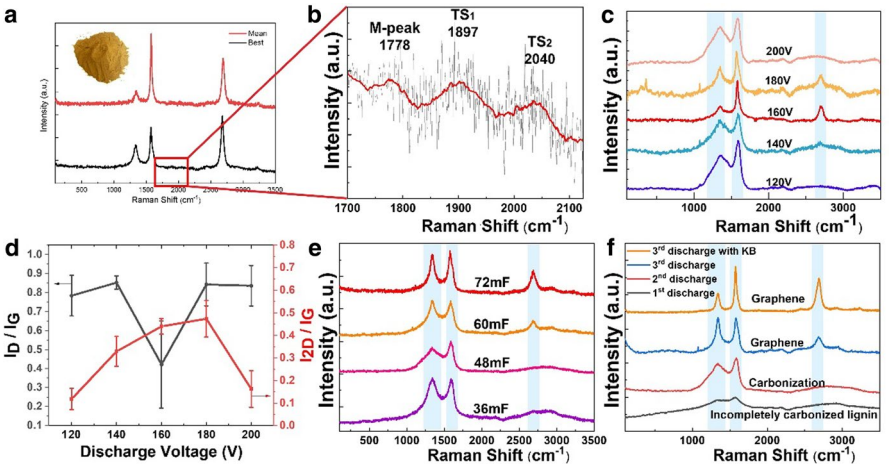

Fig. 2 Raman characterization of L-FG. **a** The products Raman spectra derived from lignin (the processing parameters of corncob powder: voltage: 160 V, capacitance: 72 mF, pressure: 1 kPa, discharge times: 5); **b** Magnification of the Raman spectrum in (**a**); **c** When the charging voltage increases from 120 to 200 V, the changes of the Raman spectrum (charging capacitance: 36 mF, pressure: 1 kPa, discharge times: 5); **d** The changes of I_{2D}/I_G and I_D/I_G in Raman spectra corresponding to (**c**); **e** When the charge capacitance increases from 36 to 72 mF, the Raman spectrum changes (charge voltage: 140 V, pressure: 1 kPa, discharge times: 5); **f** When the discharge times increases, the changes of the Raman spectrum (charging capacitance: 72 mF, pressure: 1 kPa, charge voltage: 160 V)

the voltage was continually boosted to 200 V, the I_D/I_G ratio increased, while the I_{2D}/I_G ratio decreased significantly. The reason can be explained as follows: as the high voltage caused too fast material carbonization, iron ions did not have enough time to catalyze the reactions and intercalate the graphite layers; thus, the generated L-FG has more layers and impurities. Figure 2e shows the effects of the charging capacitance on the L-FG. It was found that with an increase in capacitance from 36 to 72 mF, the stripping of graphene was effectively increased and the defects of L-FG decreased as the 2*D* peak became distinct. In addition, the discharge cycles had an impact on the process (Fig. 2f). At least three discharge cycles were required to achieve the carbonization and stripping of lignin. Interestingly, when 5 wt% of Cochin black was mixed with lignin, the quality of graphene could be increased after the same discharge cycles. It was speculated that adding a small amount of Cochin black to lignin can effectively prevent the conversion of L-FG from re-polymerization into graphite. Moreover, Cochin black can make full contact between the carbon source additive and the lignin carbon source without affecting the iron activation reaction. Increasing the concentration of $FeCl_3$ solution in the mixture also resulted in a higher intensity of the 2*D* peak of L-FG (Figure S1) due to the fact that the increased concentration of $FeCl_3$ facilitated carbonization of the raw material, however, when the concentration of $FeCl_3$ solution in the mixture was above 25 wt%, crystallized $FeCl_3$ was formed as impurities in the product. In summary, from the Raman spectra, the L-FG prepared by the flash Joule heating processing method is superior to most previously reported biomass-derived graphene [21, 22, 40–42] (Table S1).

Scanning electron microscopy (SEM) characterization showed that the graphene flakes had an obvious foam morphology (Fig. 3a, b). This is because, during the iron-catalyzed lignin conversion, porous structures were formed by the partial decomposition of lignin and evaporation of water in the raw materials [39]. High-resolution transmission electron microscopy (HRTEM) showed that the spacing between each layer was approximately 0.342 nm (Figs. 3c, d and S2), and there was AB-type stacking and turbine (rotational dislocation) stacking in the carbon atomic layer of L-FG (Fig. 3e), which is consistent with the results of Raman spectroscopy (Fig. 2b). Atomic force microscopy (AFM) revealed that the thickness of L-FG was approximately 4.1 nm (Fig. 3f, g) as there were dense nanoparticles loaded on L-FG (Fig. 3h), and the load was also inspected by TEM (Fig. 3i). After further crystal spacing measurement (Fig. 3j) and energy dispersive spectroscopy (EDS) analysis (Fig. 3k, l), it is speculated that the loaded nanoparticles were Fe_3O_4 crystals.

To further verify that Fe_3O_4 nanoparticles were loaded in the L-FG networks, high-resolution XPS analysis of the samples was performed. The x-ray photoelectron spectroscopy (XPS) results (Fig. 4a) showed that the product was composed of Fe, C, O, and N. The C1s photoelectron spectrogram showed that the binding energy had three peaks at the binding energies of 284.80, 286.41 and 288.70 eV, corresponding to sp^2 C–C, C–O/C–N and O–C=O bonds, respectively (Fig. 4b). For the photoelectron spectrum of O1s, three peaks were formed at the binding energies of 533.49, 531.61, and 531.74 eV after peak splitting, corresponding to C–O, C=O and C–O–Fe, respectively (Fig. 4c). The formation of the C–O–Fe bond could be attributed to the replacement of the oxygen-containing functional groups on the surface

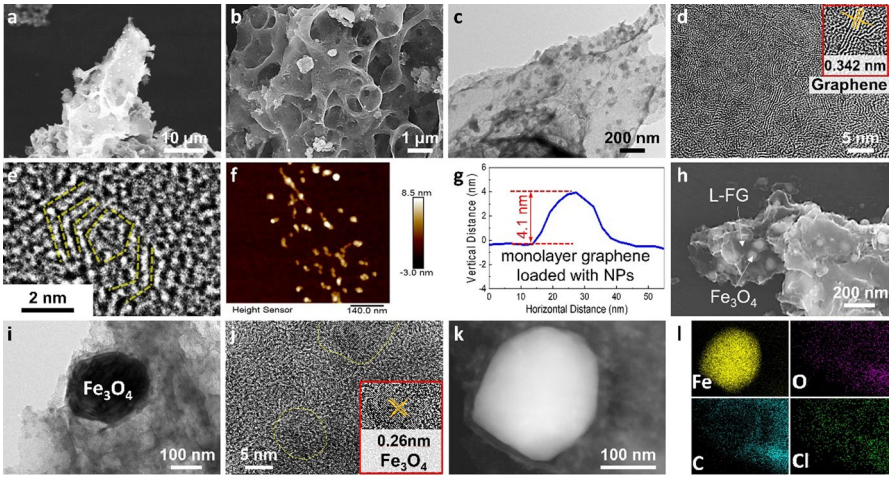

Fig. 3 Morphology and composition characterization of L-FG. **a**–**b** SEM of L-FG flasks; **c** TEM of F-LG products; **d** HRTEM of graphene layer, the insert showed the distance between L-FG parallel layers was 0.342 nm; **e** Coexistence of turbine stacked graphene and AB type stacked graphene in L-FG; **f** A typical AFM image of L-FG and the corresponding height difference shown in (**g**); **h** SEM of L-FG/Fe_3O_4 nanocomposite; **i** TEM of L-FG/Fe_3O_4 nanocomposite; **j** HRTEM of Fe_3O_4, the insert showed the distance between parallel layers of Fe_3O_4 crystal was 0.26 nm; **k** and **i** EDS element distribution of L-FG/Fe_3O_4 nanocomposite

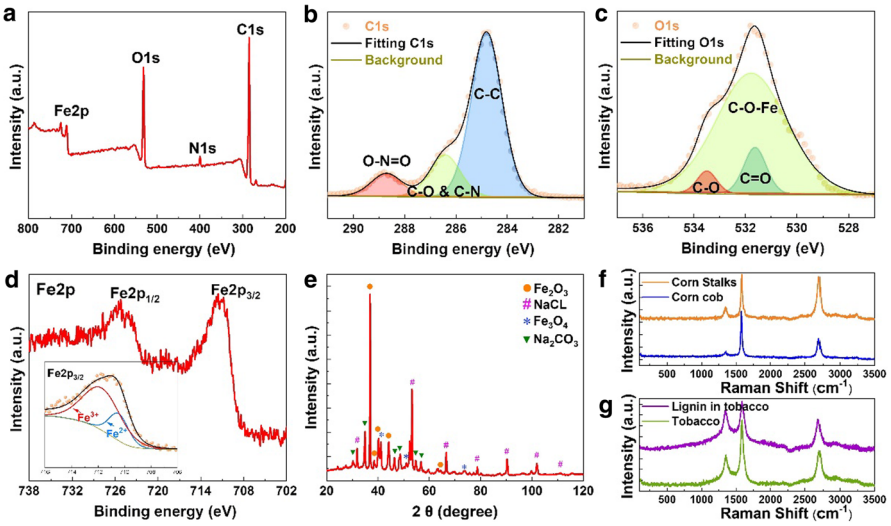

Fig. 4 XPS and XRD characterizations of L-FG/Fe_3O_4 and Raman spectra of products derived from other material sources. **a** XPS characterizations of L-FG/Fe_3O_4; **b** C1s XPS spectra of L-FG/Fe_3O_4; **c** O1s XPS spectra of L-FG/Fe_3O_4; **d** O1s XPS spectra of L-FG/Fe_3O_4; inset was Fe2p XPS spectra of L-FG/Fe_3O_4 with high-resolution spectra of $Fe2p_{3/2}$; **e** XRD characterization of L-FG/Fe_3O_4; **f** The Raman spectra of products derived from corncob powder and corn straw powder (the processing parameters of corncob powder: voltage, 180 V; pressure, 1 kPa; discharge cycles, 5); the processing parameters of corncob powder: voltage, 180 V; pressure: 1 kPa, discharge cycles, 5); **g** Raman spectra of products derived from tobacco powder (processing parameters: voltage, 140 V; pressure, 1 kPa; discharge cycles: 5)

of the porous graphene by Fe atoms [40, 43]. Figure 4d depicts the photoelectron spectrum of Fe2p, with two groups of peaks of $Fe2p_{1/2}$ and $Fe2p_{3/2}$ appearing at the bonding energies of 725.28 eV and 711.138 eV, with no obvious companion peak (satellite peak) between them, indicating that the amount of Fe_2O_3 in the product was very small [44]. Further in-depth analysis of $Fe2p_{3/2}$ peak (Fig. 4d) showed that the total peak could be divided into Fe^{3+} peak at 711.95 eV and Fe^{2+} peak at 710.59 eV. By calculating the integral area surrounded by these two small peaks and the baseline, the average ratio of Fe^{3+} to Fe^{2+} was approximately 4:1. As the ratio of Fe^{3+} and Fe^{2+} in Fe_3O_4 was 2:1, the above results showed that the L-FG-loaded particles in the product were mainly Fe_3O_4 coexisting with Fe_2O_3. The characteristic spectrum of Fe_3O_4 can be clearly observed in the x-ray diffraction (XRD) spectrum (Fig. 4e). The above results prove that during the flash Joule heating process, because of the local high temperature, $FeCl_3$ was converted into Fe_3O_4 through a series of chemical reactions which is consistent with the XPS results.

In addition, it was noted that not only commercial lignin is converted into L-FG through flash Joule heating processing but also lignin-rich raw materials, such as corn cob and corn straw (Fig. 4f). Interestingly, it was also found that when 50 wt% lignin was mixed with unusable biomass with low lignin content, such as waste tobacco, the mixture could be successfully converted into graphene (Fig. 4g), which suggests that lignin can be used as a detonator to improve the value of biomass

with low lignin content, and greatly expands the types of carbon sources that can be processed. The reason why lignin can assist the electrical discharge process can be expressed as follows: first, the strong hydrophilicity of lignin mixed with other biomass powders makes the mixture to come into full contact with the metal salt solution, providing ion transport channels and decreasing the resistance. Second, lignin can be easily ignited as its ignition point is approximately 400 °C; thus, only a small current can trigger a large amount of lignin, which is conducive to their carbonization and other biomass, providing carbides for subsequent electron transport channels.

Characterization of electromagnetic absorbing properties

Because Fe_3O_4 has a high theoretical specific capacitance, high cost-effectiveness, low toxicity, and natural abundance, it is an attractive doped material used in electromagnetic wave absorption. However, the preparation method of iron-doped electromagnetic wave-absorbing materials has the disadvantages of cumbersome and low efficiency, which cannot satisfy the needs of the rapid development of the consumer electronics market. The flash Joule heating method exploits the instantaneous high temperature and high pressure created by the flash to fulfil the raw material conversion and increase the doping density in the composites, which inspired the next exploration of the potential application of electromagnetic wave absorption.

To evaluate and better understand the mechanism of the electromagnetic (EM) absorbing properties of L-FG/Fe_3O_4 nanocomposite, L-FG/Fe_3O_4 with a loading ratio of 70 wt% in the paraffin composites were prepared, and the frequency-dependent electromagnetic parameters in the range of 2.0 to 18.0 GHz were inspected. As both the real (ε) and imaginary (ε') parts of the complex permittivity fluctuated in the frequency range of 2.0–18.0 GHz (Fig. 5a), indicating the existence of polarization behavior in the L-FG/Fe_3O_4 nanocomposite caused by the heterointerfaces, conductive carbon sheets, and defects in the L-FG/Fe_3O_4 nanocomposite [45]. There were different ferromagnetic resonance modes in the magnetic loss tangent (tan δ_μ) of the L-FG/Fe_3O_4 composites (Fig. 5a). The resonant peaks occurring at low frequencies were attributed to natural resonance from static magnetic energy, while the resonant peaks at high frequencies were attributed to the exchange resonance among the small Fe_3O_4 nanoparticles [46, 47]. Moreover, the tan δ_μ values were much smaller than the tan δ_ε values (Fig. 5a), which indicated that the dielectric loss played a major role in the EM wave absorption of the L-FG/Fe_3O_4 composite. Figure 5b shows the Cole–Cole semicircle plot of L-FG/Fe_3O_4 composites in the frequency range of 2.0–18.0 GHz. It can be seen that there were multiple semicircles, indicating that the Debye relaxation process contributed to the dielectric loss of the composite [48]. In addition, there were many irregular semicircles, which meant that there were other dielectric loss mechanisms, such as interfacial polarization, conductivity loss and dipole orientation polarization [49, 50]. Under alternating EM field conditions, with the introduction of Fe_3O_4 nanoparticles, a large number of free charges gathered at the interface between Fe_3O_4 nanoparticles

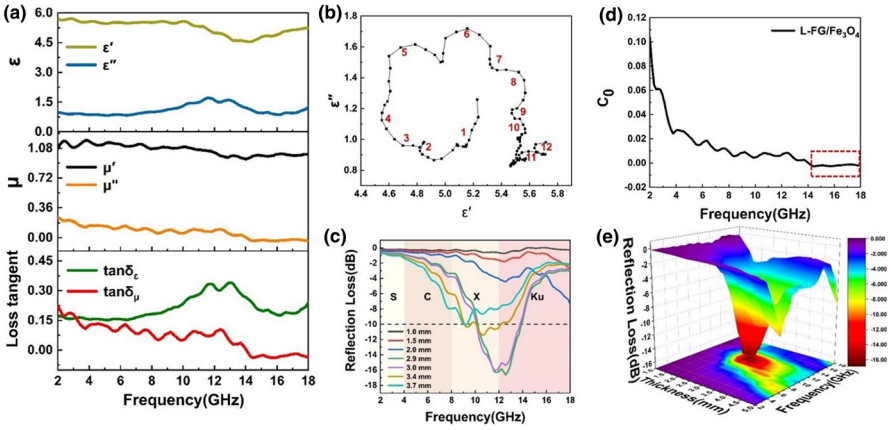

Fig. 5 Characterization of electromagnetic absorbing properties. **a** Electromagnetic parameters, the real (ε') and imaginary (ε'') parts of complex permittivity, dielectric loss tangent (tan δ_ε), the real (μ') and imaginary (μ'') parts of complex permeability, and magnetic loss tangent (tan δ_μ) of L-FG/Fe_3O_4 in a paraffin matrix with 70 wt % loading. **b** typical Cole–Cole plot and **c** C_0 curve of L-FG/Fe_3O_4 composites. **d** Reflection loss curves and **e** corresponding three-dimensional counter maps of L-FG/Fe_3O_4 nanocomposite

and carbon flakes, as well as the interface between the L-FG/Fe_3O_4 composite and paraffin, creating sufficient interfacial polarization. In addition to this, as revealed by XPS, the L-FG/Fe_3O_4 composite had many surface functional groups and localized defects such as C=O, C–O, and dangling bonds, which contributed to conductivity loss.

For the magnetic loss, the eddy current loss (C_0) curve for the L-FG/Fe_3O_4 nanocomposite remained nearly constant with an increase in frequency in the range of 14.2–18.0 GHz (Fig. 5c), shows that the magnetic loss was dominated by the eddy current loss in the high-frequency range, together with natural resonance and exchange resonance.

Figure 5d, e shows the calculated reflection loss (RL) and the corresponding three-dimensional counter maps of the L-FG/Fe_3O_4 nanocomposite in the frequency range of 2.0–18.0 GHz at different thicknesses. The minimum RL value of L-FG/Fe_3O_4 nanocomposite reached −16.6 dB at 12.6 GHz with the thickness d of 2.9 mm, and the effective absorption bandwidth almost reached 3.7 GHz (10.2–13.8 GHz). The effective absorbing bandwidth involves the X-band and Ku-band. It can be seen that the attenuation peaks gradually shift to the low-frequency region with an increase in the absorber thickness, which can be explained by the quarter-wavelength attenuation principle. Moreover, the qualified microwave absorption of L-FG/Fe_3O_4 nanocomposite covered up a region of 4.8 GHz (9.0–13.8 GHz) by increasing the thickness from 2.9 to 3.9 mm. The results clearly showed that the sample obtained by the wet-flash method had EM wave absorption capability in both absorption intensity and qualified bandwidth.

Conclusion

In this work, a flash Joule heating method was proposed to fabricate high-quality L-FG/Fe_3O_4 nanocomposites from a mixture of lignin and ferric chloride solution. The results showed that the presence of iron trichloride promoted the effective intercalation and uniform exfoliation of cations on lignin carbons resulted in at high temperatures, enabling the preparation of lignin-derived graphene with few layers and defects from nonconducting lignin by flash Joule heating, as verified by Raman and high-resolution TEM characterization. More importantly, the Fe_3O_4 nanoparticles were produced and in situ loaded on the lignin-derived graphene sheets as confirmed by TEM and XRD characterization. The characterization of electromagnetic absorption properties showed that the L-FG/Fe_3O_4 nanocomposites achieved a minimum RL value of −16.6 dB and a qualified microwave absorption region of 4.8 GHz, which indicated a significant increase in the utilization of lignin. Thus, the proposed method provides a feasible and economical approach for the fabrication of high-performance graphene-based functional composites and can be extended to general low-value biomass processing.

Supplementary Information The online version contains supplementary material available at https://doi.org/10.1007/s11164-022-04883-7.

Author contributions YC: Conceptualization, Methodology, Investigation, Writing—Reviewing and Editing; ZH: Investigation, Writing—original draft; SD: Investigation, Writing—original draft; MW: Investigation, Writing—original draft; HL: Investigation; MH: Investigation; XC: Investigation, Supervision; JG: Investigation; LW: Investigation, Writing—Reviewing and Editing; C-PW: Supervision. All authors reviewed the manuscript.

Funding This work was supported by the National Natural Science Foundation of China [Grant No. 51975127, U20A6004], National Key R&D Program of China Research [Grant No. 2022YFB4701002] and Development Program of Guangdong Province [Grant No. 2020A0505140008]. Thanks to the Guangdong University of Technology Analysis and Test Center for the field emission scanning electron microscope (SU8220, Hitachi).

Declarations

Conflict of interests The authors declare that they have no conflict of interest.

References

1. L.L. Dai, Y.P. Wang, Y.H. Liu, R. Ruan et al., Renew. Sust. Energ. Rev. **107**, 51 (2019)
2. C.J. Chen, Y.D. Kuang, S.Z. Zhu, I. Burgert et al., Nat. Rev. Mater. **5**, 9 (2020)
3. D.C. Shi, Y. Chen, Z.J. Li, S.K. Dong et al., Small Methods **6**, 8 (2022)
4. A.J. Ragauskas, G.T. Beckham, M.J. Biddy, R. Chandra et al., Science **344**, 6185 (2014)
5. C. Liu, P.C. Luan, Q. Li, Z. Cheng et al., Adv. Mater. **33**, 28 (2021)
6. B.M. Upton, A.M. Kasko, Chem. Rev. **116**, 4 (2016)
7. M. Yi, Z.G. Shen, J. Mater. Chem. A **3**, 22 (2015)
8. Y. Hernandez, V. Nicolosi, M. Lotya, F.M. Blighe et al., Nat. Nanotechnol. **3**, 9 (2008)
9. D.C. Marcano, D.V. Kosynkin, J.M. Berlin, A. Sinitskii et al., ACS Nano **4**, 8 (2010)
10. K. De Silva, H.H. Huang, R. Joshi, M. Yoshimura, Carbon **166**, 74 (2020)

11. S. Stankovich, D.A. Dikin, R.D. Piner, K.A. Kohlhaas et al., Carbon **45**, 7 (2007)
12. H. Tetlow, J.P. de Boer, I.J. Ford, D.D. Vvedensky et al., Phys. Rep. **542**, 3 (2014)
13. B. Jiang, S.W. Wang, J.Y. Sun, Z.F. Liu, Small **17**, 37 (2021)
14. Z.Y. Ding, T.Q. Yuan, J.L. Wen, X.F. Cao et al., Carbon **158**, 690 (2020)
15. W. Fang, S. Yang, X.L. Wang, T.Q. Yuan et al., Green Chem. **19**, 8 (2017)
16. G.D. Ruan, Z.Z. Sun, Z.W. Peng, J.M. Tour, ACS Nano **5**, 9 (2011)
17. K. Fujisawa, Y. Lei, C. de Tomas, I. Suarez-Martinez et al., Carbon **142**, 78 (2019)
18. Y. Chen, B. Xie, J.Y. Long, Y.C. Kuang et al., Adv. Mater. **33**, 44 (2021)
19. F. Mahmood, H.W. Zhang, J. Lin, C.X. Wan, ACS Omega **5**, 24 (2020)
20. W.L. Zhang, Y.J. Lei, F.W. Ming, Q. Jiang et al., Adv. Energy Mater. **8**, 27 (2018)
21. Y. Chen, J.Y. Long, B. Xie, Y.C. Kuang et al., ACS Appl. Mater. Inter. **14**, 3 (2022)
22. Y. Chen, J.Y. Long, S. Zhou, D.C. Shi et al., Small Methods **3**, 10 (2019)
23. Y.H. Li, J.Y. Long, Y. Chen, Y. Huang et al., Adv. Mater. **34**, 21 (2022)
24. M.G. Stanford, K.V. Bets, D.X. Luong, P.A. Advincula et al., ACS Nano **14**, 10 (2020)
25. D.X. Luong, K.V. Bets, W.A. Algozeeb, M.G. Stanford et al., Nature **577**, 7792 (2020)
26. K.M. Wyss, D.X. Luong, J.M. Tour, Adv. Mater. **34**, 8 (2022)
27. K.M. Wyss, W.Y. Chen, J.L. Beckham, P.E. Savas et al., ACS Nano **16**, 5 (2022)
28. P.A. Advincula, D.X. Luong, W.Y. Chen, S. Raghuraman et al., Carbon **178**, 649 (2021)
29. XD Liu, Y Huang, L Ding, XX Zhao et al., J. Mater. Sci. Technol. **72**, (2021)
30. Y.A. Yang, L. Xia, T. Zhang, B. Shi et al., Chem. Eng. J. **352**, 510 (2018)
31. T.S. Wang, Z.H. Liu, M.M. Lu, B. Wen et al., J. Appl. Phys. **113**, 2 (2013)
32. Y.L. Zhong, Z. Tian, G.P. Simon, D. Li, Mater. Today **18**, 2 (2015)
33. A.C. Ferrari, J.C. Meyer, V. Scardaci, C. Casiraghi et al., Phys. Rev. Lett. **97**, 18 (2006)
34. H.Y. Quan, B.C. Cheng, Y.H. Xiao, S.J. Lei, Chem. Eng. J. **286**, 165 (2016)
35. L.M. Malard, M.A. Pimenta, G. Dresselhaus, M.S. Dresselhaus, Phys. Rep. **473**, 5–6 (2009)
36. S.H. Yang, X.F. Song, P. Zhang, L.A. Gao, J. Mater. Chem. A **1**, 45 (2013)
37. A.C. Ferrari, Solid State Commun. **143**, 1–2 (2007)
38. R.Z. Li, Y.M. Wang, C. Zhou, C. Wang et al., Adv. Funct. Mater. **25**, 33 (2015)
39. W.A. Algozeeb, P.E. Savas, D.X. Luong, W.Y. Chen et al., ACS Nano **14**, 11 (2020)
40. L.S. Xu, C. Cheng, C.L. Yao, X.J. Jin, Org. Electron. **78**, 105407 (2020)
41. Z.Y. Ding, F.F. Li, J.L. Wen, X.L. Wang et al., Green Chem. **20**, 6 (2018)
42. R.Q. Ye, Y. Chyan, J.B. Zhang, Y.L. Li et al., Adv. Mater. **29**, 37 (2017)
43. F. Temerov, A. Belyaev, B. Ankudze, T.T. Pakkanen, J. Lumin. **206**, 403 (2019)
44. R. Trusovas, K. Ratautas, G. Raciukaitis, G. Niaura, Appl. Surf. Sci. **471**, 154 (2019)
45. B.W. Deng, Z. Xiang, J. Xiong, Z.C. Liu et al., Nano-micro Lett. **12**, 1 (2020)
46. Y.Q. Wang, H.G. Wang, J.H. Ye, L.Y. Shi et al., Chem. Eng. J. **383**, 130079 (2020)
47. D.W. Liu, Y.C. Du, P. Xu, N. Liu et al., J. Mater. Chem. C **7**, 17 (2019)
48. Z.L. Zhang, Y.Y. Lv, X.Q. Chen, Z. Wu et al., J. Magn. Magn. Mater. **487**, 165334 (2019)
49. P.P. Zhou, X.K. Wang, Z. Song, M. Wang et al., Carbon **176**, 279 (2021)
50. Y. Qiu, Y. Lin, H.B. Yang, L. Wang et al., Chem. Eng. J. **383**, 123207 (2020)